

# Variability of stalagmite-inferred Indian monsoon precipitation over the past 252,000 y

Cai, Yanjun; Fung, Inez Y.; Edwards, R. Lawrence; An, Zhisheng; Cheng, Hai; Lee, Jung-Eun; Tan, Liangcheng; Shen, Chuan-Chou; Wang, Xianfeng; Day, Jesse A.; Zhou, Weijian; Kelly, Megan J.; Chiang, John C. H.

2015

Cai, Y., Fung, I. Y., Edwards, R. L., An, Z., Cheng, H., Lee, J. E., et al. (2015). Variability of stalagmite-inferred Indian monsoon precipitation over the past 252,000 y. *Proceedings of the National Academy of Sciences of the United States of America*, 112(10), 2954-2959.

<https://hdl.handle.net/10356/107132>

<https://doi.org/10.1073/pnas.1424035112>

---

© 2015 The Author(s) (Published by National Academy of Sciences). This is the author created version of a work that has been peer reviewed and accepted for publication by *Proceedings of the National Academy of Sciences of the United States of America*, The Author(s) (Published by National Academy of Sciences). It incorporates referee's comments but changes resulting from the publishing process, such as copyediting, structural formatting, may not be reflected in this document. The published version is available at: [<http://dx.doi.org/10.1073/pnas.1424035112>].

**Classification:** Earth, Atmospheric, and Planetary Sciences in **Physical Sciences**

## **Variability of stalagmite-inferred Indian Monsoon precipitation over the past 252,000 years**

Yanjun Cai<sup>a,b\*</sup> Inez Fung<sup>c\*</sup> R. Lawrence Edwards<sup>d</sup> Zhisheng An<sup>a,b</sup> Hai Cheng<sup>b,d</sup> Jung-Eun Lee<sup>e</sup>  
Liangcheng Tan<sup>a</sup> Chuan-Chou Shen<sup>f</sup> Xianfeng Wang<sup>g</sup> Jesse A. Day<sup>c</sup> Weijian Zhou<sup>a</sup>  
Megan Kelly<sup>d</sup> John C. H. Chiang<sup>c</sup>

<sup>a</sup>State Key Lab of Loess and Quaternary Geology, Institute of Earth Environment,  
Chinese Academy of Sciences, Xi'an 710075, China

<sup>b</sup>Institute of Global Environmental Change, Xi'an Jiaotong University, Xi'an 710049, China

<sup>c</sup>Center for Atmospheric Sciences, University of California, Berkeley, CA 94720, USA

<sup>d</sup>Department of Earth Sciences, University of Minnesota, Minneapolis, Minnesota 55455, USA

<sup>e</sup>Department of Geological Sciences, Brown University, Providence, RI 02912, USA

<sup>f</sup>High-Precision Mass Spectrometry and Environment Change Laboratory (HISPEC),  
Department of Geosciences, National Taiwan University, Taipei 106, Taiwan

<sup>g</sup>Earth Observatory of Singapore, Nanyang Technological University, Singapore

\*Correspondence to:

Inez Fung, ifung@berkeley.edu, Tel: +1-510-643-9367, Fax: +1-510-643-9980

Yanjun Cai, yanjun\_cai@ieecas.cn, Tel: +86-29-88323194, Fax: +86-29-88320456

**Keywords:** Indian summer monsoon, stalagmite,  $\delta^{18}\text{O}$ , precipitation, glacial-interglacial, isotope-enabled circulation modeling, sea level changes.

**Abstract:**

A speleothem  $\delta^{18}\text{O}$  record from Xiaobailong cave in southwest China characterizes changes in summer monsoon precipitation in Northeastern India, the Himalayan foothills, Bangladesh and northern Indochina over the last 252 kyr. This record is dominated by 23-kyr precessional cycles punctuated by prominent millennial-scale oscillations that are synchronous with Heinrich events in the North Atlantic. It also shows clear glacial-interglacial (G-I) variations that are consistent with marine and other terrestrial proxies, but are different from the cave records at East China. Corroborated by isotope-enabled global circulation modeling, we hypothesize that this disparity reflects differing changes in atmospheric circulation and moisture trajectories associated with climate forcing as well as with associated topographic changes during glacial periods, in particular redistribution of air mass above the growing ice sheets and the exposure of the “land bridge” in the Maritime continents in the western equatorial Pacific.

**Significance Statement**

This paper presents a new long speleothem  $\delta^{18}\text{O}$  time series from Xiaobailong cave in southwest China that characterizes changes in a major branch of Indian summer monsoon precipitation over the last 252 kyrs. This record shows not only 23-kyr precessional cycles punctuated by prominent millennial-scale weak monsoon events synchronous with Heinrich events in the North Atlantic, but also clear glacial-interglacial (G-I) variations that are consistent with marine records but different from the cave records at East China. The speleothem records of Xiaobailong and other caves in East China show that the relationship between the Indian and the East Asian summer monsoon precipitation is not invariant, but varies on different time scales depending on the nature and magnitude of the climate forcing.

The Indian summer monsoon (ISM), a key component of tropical climate, provides vital precipitation to southern Asia. The ISM is characterized by two regions of precipitation maxima: a narrow coastal region along the Western Ghats, denoted by ISM<sub>A</sub>, with moisture from the Arabian Sea; and a broad “Monsoon Zone” around 20°N in north-eastern India, denoted by ISM<sub>B</sub>, where storms emanate from the Bay of Bengal and whose rainfall variability is well correlated with that of “All India” rainfall (1). Multiple proxies obtained from Arabian Sea sediments have revealed the variability of summer monsoon winds on timescales of 10<sup>1</sup>-10<sup>5</sup> years (e.g., 2-6). Our understanding of the paleo-precipitation variability of ISM<sub>B</sub> remains incomplete, due to the scarcity of long and high-resolution records. Here we present a 252,000-year long speleothem  $\delta^{18}\text{O}$  record from Xiaobailong cave, southwest China and characterize variability in the ISM<sub>B</sub> precipitation on multiple time scales.

Xiaobailong (XBL, “Little White Dragon”) cave is located in Yunnan Province, southwestern China, near the southeastern edge of the Tibetan Plateau (103°21'E, 24°12'N, ~1500m above sea level, Fig. S1). Local climate is characterized by warm/wet summers and cool/dry winters. The mean annual precipitation of ~960 mm (1960-2000) falls mostly from June through September (~80%) (Fig. S2), indicating the summer monsoon rainfall dominates the annual precipitation at the cave site. The temperature in the cave is 17.2 °C, close to local mean annual air temperature (17.3 °C).

Eight stalagmites were collected from the inner chamber (~350 m from the entrance) of the cave, where humidity is ~100% and ventilation is confined to a small crawl-in channel to the outer chamber. One hundred and four <sup>230</sup>Th dates were determined on inductively coupled plasma mass spectrometers with typical relative error in age (2 $\sigma$ ) of less than 1% (SI Materials and Methods, Table S1, Fig. S3 and Fig. S4). The ages vary monotonically with depth in the stalagmites (Fig. S4) and the <sup>230</sup>Th dates were linearly interpolated to establish chronologies. Measurements of calcite  $\delta^{18}\text{O}$  ( $\delta^{18}\text{O}_c$ ) were made by isotope ratio mass spectrometer on a total of 1896 samples from the eight stalagmites (SI Materials and Methods, Table S2). By matching the chronology established by the absolute <sup>230</sup>Th dates, the  $\delta^{18}\text{O}_c$  time series of the different stalagmites were combined to form a single time series. The resulting XBL record (Fig. 1) covers

the past 252,000 years, with an average resolution of 70 yrs between 5.0 and 80.0 thousand years before present (ka BP, before 1950AD) and 260 yrs between 80.0 and 252.0 ka BP, excluding several interruptions of calcite deposition, e.g. during the periods of 52.4-59.8, 164.0-167.2, 204.5-214.1 and 216.8-222.2 ka BP.

In principle, variations in calcite  $\delta^{18}\text{O}_c$  of stalagmites could capture variations of  $\delta^{18}\text{O}$  in precipitation ( $\delta^{18}\text{O}_p$ ), cave temperature which is close to the surface annual mean temperature, and kinetic loss of  $\text{CO}_2$  and evaporation of water during the calcite deposition. We rule out these kinetic fractionation processes, as  $\delta^{18}\text{O}_c$  records from different stalagmites in XBL cave agree with one another within quoted dating errors over contemporaneous growth periods (Fig. 1), and  $\delta^{13}\text{C}$  records also replicate across speleothems within the cave, suggesting dominant climate control (SI Materials and Methods, Fig. S5). Furthermore, the XBL  $\delta^{18}\text{O}_c$  records broadly resemble, on precessional and millennial timescales for overlapping periods (Fig. 1), speleothem records from Hulu Dongge Sanbao and Linzhu caves (HL-DG-SB-LZ) in East China (13), providing another robust replication test and indicating that the  $\delta^{18}\text{O}_c$  signal in these stalagmites is primarily of climatic origin. The range of calcite  $\delta^{18}\text{O}_c$  change at XBL is  $\sim 8.0\text{‰}$  over 252 kyr. Since temperature-dependent fractionation between calcite and water is likely to be below  $2\text{‰}$  (estimated using  $\sim -0.23\text{‰}/^\circ\text{C}$  (14), and assuming a maximum  $8^\circ\text{C}$  difference between glacial and inter-glacial periods (15)), the shifts in stalagmite  $\delta^{18}\text{O}_c$  are primarily due to changes in meteoric precipitation  $\delta^{18}\text{O}_p$  at the cave site.

We interpret XBL  $\delta^{18}\text{O}_c$  as an index of  $\text{ISM}_B$  rainfall at a region denoted the Monsoon Zone-B, which encompasses the Monsoon Zone of northeastern India (1), the Himalayan foothills, Bangladesh and northern Indochina. Firstly, the Bay of Bengal supplies the bulk of moisture to both the Monsoon Zone-B and to XBL across the Indochinese Peninsula; and present-day summer precipitation of the two regions are positive correlated (Fig. S6). Secondly, multiple climate model simulations show similar 850 hPa wind trajectories for these two regions for both present-day and LGM, suggesting moisture paths from the Bay of Bengal to XBL were relatively stable in the past (Fig. S7). Thirdly, the XBL  $\delta^{18}\text{O}_c$  record shows good agreement ( $r=0.56$ ), over the past 100 ka, with the salinity proxy, and by inference fluvial runoff proxy, reconstructed from ODP core 126 KL in the Bay of Bengal (16), with decreased  $\delta^{18}\text{O}_c$  values at XBL corresponding with lower salinity and hence increased precipitation, and vice versa (Fig. S8). We hereafter

define a ‘strong’ ISM<sub>B</sub> as an increase of precipitation over the Monsoon Zone-B, and a corresponding decrease of  $\delta^{18}\text{O}_c$  value at XBL (SI Materials and Methods).

### ***Variability of Indian summer monsoon***

The dominant variability of XBL  $\delta^{18}\text{O}_c$  aligns well with Northern Hemisphere summer (June-July-August) insolation (NHSI) variation on a  $\sim 23$  kyr cycle associated with precession of the Earth’s orbit. Low  $\delta^{18}\text{O}_c$  values, heavier precipitation or stronger ISM<sub>B</sub> are associated with higher NHSI, and vice versa. The record is also punctuated by many millennial-scale abrupt events (Fig. 1, Fig. S8). During the last glacial period (from  $\sim 75$  to  $\sim 20$  ka BP), when the XBL  $\delta^{18}\text{O}_c$  record has a mean resolution as high as  $\sim 70$  yr, these abrupt events ( $\sim 15.9$ ,  $\sim 24.3$ ,  $\sim 30.1$ ,  $\sim 39.3$ ,  $\sim 48.2$ ,  $\sim 62.0$  ka BP) are marked by consistent increases of  $\delta^{18}\text{O}_c$ , or weaker ISM<sub>B</sub>, that are aligned with Heinrich events (17), thus suggesting a link between ISM and climate change in the North Atlantic (4, 7). However, decrease of  $\delta^{18}\text{O}_c$  during apparent warm Dansgaard/Oeschger periods is indistinguishable, likely due to the resolution of the record.

On glacial-interglacial ( $\sim 100$  kyr) time scales, the XBL calcite  $\delta^{18}\text{O}_c$  values vary between  $\sim -9\%$  and  $\sim -11\%$  during glacial periods (e.g. 20-75 ka BP), and are much higher than the  $\sim -14\%$  of the interglacial optimum periods (e.g., high insolation periods within 75-130 ka BP) (Fig. 1), indicating relatively weak ISM during glacial periods. This is in agreement with other paleomonsoon records (2, 18), especially Chinese loess records that feature a significant glacial-interglacial cycle from 600 ka BP to the present (19).

To separate XBL  $\delta^{18}\text{O}_c$  into its modes of variability, we applied Ensemble Empirical Mode Decomposition (EEMD), a new noise-assisted method (20) for analyzing non-linear non-stationary time series. Unlike Fourier or wavelet analysis, which decomposes a stationary time series into a chosen set of known functions and seeks each of their global (over the entire time series) amplitudes, EEMD determines, without prior assumptions, instantaneous frequencies and instantaneous amplitudes via a sifting algorithm (20, 21, 22). The resulting components are ordered by time scale, from the shortest to the longest (Fig. S9). For the XBL record, the dominant variability (47.3% of the total variance) is captured by the component C9-10, and shows variability with a  $\delta^{18}\text{O}_c$  range of  $\sim 5\%$  that is coincident with NHSI at the precessional

time scale ( $\sim 23$ kyr) (Fig 2). The next component (C11-13) captures 33% of the variance, with a  $\delta^{18}\text{O}_c$  range of  $\sim 4\text{‰}$ . It peaks around 120 ka and has a broad minimum during the ice ages.

Millennial scale variability (C6-8) has a  $\delta^{18}\text{O}_c$  range of  $\sim 4\text{‰}$  and captures 19% of the variance.

A similar EEMD analysis was applied to the HL-DG-SB-LZ calcite  $\delta^{18}\text{O}_c$  time series from eastern China (9-11, 13, Figure 2). The dominant modes of variability at the East China caves are on precessional (69% of variance,  $\delta^{18}\text{O}_c$  range  $\sim 6\text{‰}$ ) and millennial (19% of the variance,  $\delta^{18}\text{O}_c$  range  $\sim 4\text{‰}$ ) time scales. While these modes are similar to those at XBL, on glacial-interglacial time scales the HL-DG-SB-LZ  $\delta^{18}\text{O}_c$  range is only  $\sim 1\text{‰}$  compared to  $\sim 4\text{‰}$  at XBL and captures only 11% of the variance.

The correlation coefficient ( $r$ ) between XBL and HL-DG-SB-LZ EEMD components is 0.8 on precessional time scale. The synchrony between the ISM<sub>B</sub> and East Asian Summer Monsoon (EASM), as revealed by EEMD analysis of the long XBL and HL-DG-SB-LZ  $\delta^{18}\text{O}_c$  time series (Fig. 1 and 2), confirms previous observations in intermittent speleothem records from South Asia and East Asia (8, 23-26), thus strengthening the hypothesis that both the Indian and East Asian summer monsoons vary directly in response to changes in NHI on precessional time scales (27, 13). Our results contradict the hypothesis that winter precipitation affects the phase of EASM cave  $\delta^{18}\text{O}_c$  signals (28) on precessional time scale, since changes in  $\delta^{18}\text{O}_c$  are synchronous between East China sites and XBL, where the contribution of winter precipitation is negligible. Instead, we point out that the phase of speleothem  $\delta^{18}\text{O}_c$  relative to the insolation signal could vary by up to several thousand years, depending on the choice of reference month(s).

There is no significant correlation ( $r=0.2$ ) between XBL and HL-DG-SB-LZ  $\delta^{18}\text{O}_c$  on millennial time scale, even though both show increased  $\delta^{18}\text{O}_c$  values that are synchronous with Heinrich events within quoted errors. Changes in the North Atlantic Ocean during Heinrich events led to circulation changes over the entire Northern Hemisphere (29), and moisture from the Indian Ocean is hypothesized to dominate the isotope composition of precipitation in East Asia (e.g. 29-31). However, two features may preclude attaining a significant correlation on millennial timescales between the two records: first, dating uncertainty in each record may affect the alignment between the two records, especially during the penultimate glacial-interglacial period; and second, several gaps in the XBL record are filled by linear interpolation and do not contain information on millennial timescales. If we correlate the two records at millennial timescales

only for the period from 5.4 to 52.4 ka BP where both records are complete and the errors are relatively small, the correlation increases to  $r=0.46$  which is significant at the 0.01 level.

### ***Different responses of South and East Asian speleothem $\delta^{18}\text{O}$ on glacial-interglacial timescales***

Significant differences exist between the XBL and HL-DG-SB-LZ  $\delta^{18}\text{O}_c$  records. For example, the glacial-interglacial ranges, e.g., between marine isotope stages (MIS) 5 and 3, in  $\delta^{18}\text{O}_c$  are large and distinct at XBL and barely discernible in the HL-DG-SB-LZ record (Fig. 1, 2).

Furthermore, between MIS 5a and 5c, XBL shows an increasing trend, opposite to that in HL-DG-SB-LZ. The EEMD analysis also shows no significant relationship between XBL and East China speleothem  $\delta^{18}\text{O}_c$  records on the  $\sim 100$  kyr glacial-interglacial time scale: the correlation coefficient between the two EEMD components is only  $\sim 0.1$ .

To understand the glacial-interglacial differences, we analyze the output of two runs of an isotope-enabled general circulation model with prescribed boundary conditions both for present day and for the LGM (SI Materials and Methods, 32). In the model,  $\delta^{18}\text{O}$  of ocean water was specified to be 0.5‰ for the present-day and 1.7‰ during the LGM because of the loss of water depleted in heavy isotopes to the ice sheets. Relative to present day, LGM summer precipitation decreased substantially over the Indian Ocean and Indian subcontinent, but stratiform precipitation increased over the exposed continental shelf of East Asia (Fig. 3a). Similarly, LGM precipitation  $\delta^{18}\text{O}_p$  was higher, by 2.0–4.0‰, throughout the Indian Ocean and South Asia (including the XBL cave site), but showed either minor increases or decreases of 1.0–2.0‰ in East Asia (East of 105°E) (Fig. 3b).

To estimate the calcite  $\delta^{18}\text{O}_c$  from the modeled temperature and precipitation  $\delta^{18}\text{O}_p$ , we first used a temperature fractionation of calcite  $\delta^{18}\text{O}_c$  of  $\sim -0.23\text{‰}/^\circ\text{C}$  and modeled LGM temperature decreases at the cave sites, i.e.,  $\sim 4^\circ\text{C}$  at XBL and  $\sim 6^\circ\text{C}$  at HL-DG-SB-LZ (Fig. S10), yielding a temperature-based  $\sim 1.0\text{‰}$  and  $\sim 1.5\text{‰}$  increase in  $\delta^{18}\text{O}_c$  during the LGM, at XBL and at HL-DG-SB-LZ, respectively. The combined temperature and precipitation effect would yield a LGM calcite  $\delta^{18}\text{O}_c$  increase of  $\sim 3.0\text{--}5.0\text{‰}$  ( $\sim 2.0\text{--}4.0 + 1.0\text{‰}$ ) at XBL, and little change ( $\sim 0.5$  to  $-0.5\text{‰}$ , or  $-1.0$  to  $-2.0\text{‰} + 1.5\text{‰}$ ) at HL-DG-SB-LZ caves. The model results are thus consistent with the observations in speleothem records.



Our model, like other models in the Paleoclimate Modeling Intercomparison Project Phase II (PMIP2) suite (15), shows a major trajectory of moisture advection from the northern reaches of the Bay of Bengal across the Yunnan Plateau and northern Indochina to XBL for the present day and the LGM (Fig. 4). Due to the lower temperatures during the LGM, there was less moisture transport and precipitation along this path (Fig. 3a and Fig. 4). Together with the more enriched source water, LGM vapor  $\delta^{18}\text{O}$  ( $\delta^{18}\text{O}_v$ ) was less depleted (Fig. 4b, 4c) and  $\delta^{18}\text{O}_p$  was more enriched (+2.0~4.0‰) at XBL.

In contrast, the paths for moisture advection to East China are more varied, with three major paths to the region, a pattern consistent with modern observations (33): from the Arabian Sea across the southern Bay of Bengal (the Indian Ocean path), from the South China Sea and tropical Pacific, and from the North Pacific (Fig. 4, Fig. 5). Atmospheric circulation was different during the LGM, not only because of lower abundance of greenhouse gases, lower sea surface temperatures and expanded sea ice coverage, but also because of altered topography with elevated continental glaciers and lowered sea level exposing new land surfaces. Off the Pacific coast of Asia, sea level during the LGM was ~120 meters lower than today (34), exposing the “land bridge”, the continental shelf around the Gulf of Thailand, South China Sea and East China Sea, while there were only minor changes around the Bay of Bengal.

During the LGM, the Indian Ocean path of moisture advection to East China was shifted slightly equatorward and strengthened over the southern Bay of Bengal. This path contributed ~30% and 15% of the LGM precipitation at Dongge and Hulu, respectively (29). The trajectory passed over the “land bridge”, where evaporation was reduced and stratiform precipitation increased relative to the present day (Fig. 3a), contributing to depleted  $\delta^{18}\text{O}_v$  of the vapor (Fig. 4b, 4c) and depleted  $\delta^{18}\text{O}_p$  values downstream at Dongge, Hulu and other East China cave sites.

Moisture advection to the Hulu cave region in East China was more complicated during the LGM. Moisture advection from the South China Sea and the tropical Pacific was significantly increased compared to the present day, despite the ~40% decrease in atmospheric water vapor in the LGM atmosphere (7%/K for 6K decrease) (Fig. S11). This is because southerly and southeasterly winds increased in response to a strengthened east-west pressure gradient between the continent and the Pacific Ocean as well as to the enhancement of the subtropical high pressure system in the Pacific Ocean (Figure 5), resulting from the redistribution of air mass from the

continents to the oceans as glaciers grew. This increase in moisture flux was countered by an anomalous north-easterly flow from the North Pacific, as a result of greater surface pressure increase over the Bering Sea ( $\sim 10$  hPa) than over the mid-latitude ocean ( $\sim 5$  hPa) (Fig. 5). This pattern of pressure difference induced anomalous south-easterly and north-easterly flows towards Eastern China and together increased the moisture from the Pacific by  $\sim 10\%$  (Fig. S11). As a result of the circulation changes, moisture convergence over the region of the East China caves ( $110-120^\circ\text{E}$ ,  $20-35^\circ\text{N}$ ) increased and precipitation increases followed (Fig. S11). In East China, the decrease in  $\delta^{18}\text{O}_v$  from increased precipitation competed with the increase in  $\delta^{18}\text{O}$  of the ocean source, resulting in little change in  $\delta^{18}\text{O}_p$  at HL-DG-SB-LZ.

Taken all together, the circulation changes together with more enriched ocean water result in an unchanged and/or slightly depleted  $\delta^{18}\text{O}_p$  over the East China during the LGM, consistent with the observations at cave sites in East China during glacial periods.

### ***Concluding remarks***

The XBL  $\delta^{18}\text{O}_c$  record documents the variability of the  $\text{ISM}_B$  precipitation on glacial-interglacial, precessional, and millennial time scales over the last 252,000 years. Unlike speleothem records from East China, XBL is concordant with records of the  $\text{ISM}_B$  from marine sediments and loess records on glacial-interglacial time scale.

Our modeling results show that glacial-interglacial changes in atmospheric circulation and rainfall are manifested in isotopically different ways at XBL and in East China, with much depleted precipitation  $\delta^{18}\text{O}_p$  during interglacial than glacial at XBL versus nearly unchanged precipitation  $\delta^{18}\text{O}_p$  in East China. We further suggest that reduced evaporation over exposed continental shelf during the LGM could have contributed to the depleted precipitation  $\delta^{18}\text{O}_p$  downstream at some of the cave sites in East China.

Our study, along with other paleoclimate modeling studies, puts forth pieces of the puzzle of how regional circulation and hydrology respond to different climate forcings or perturbations. The model results taken altogether show that variations in  $\delta^{18}\text{O}_p$ , and by inference,  $\delta^{18}\text{O}_c$  of

speleothems, reflect regional and hemispheric scale variations in vapor flux as well as in situ condensation and evaporation in the atmospheric column (42-45).

The Indian Ocean moisture path to East Asia appears robust, even though the magnitude of the fluxes vary, in the comparison of the present-day and the LGM here, and in a comparison of the LGM with or without the Heinrich perturbation (29). In this study, changes in the tropical and North Pacific moisture fluxes dominated the  $\delta^{18}\text{O}_p$  changes in East China during the LGM. Our result that the land bridge exposed during the LGM led to enhanced summer large-scale stratiform precipitation is not inconsistent with the reduction in annual mean convection over the Sunda Shelf (e.g. 43). While the complexity of circulation changes in influencing precipitation changes of a site or a region is not a surprise, the long speleothem records, such as the XBL  $\delta^{18}\text{O}_c$  data presented here, present unique opportunities for improving climate models and for testing hypotheses about past hydro-climate changes.

## **Methods**

### **U-series dating and stable isotope analysis**

All stalagmites were cut into halves along the growth axis and their surfaces were polished. Fig. S4 illustrates images of the stalagmites and the  $^{230}\text{Th}$  dating positions. Subsamples were drilled along growth axes for  $^{230}\text{Th}$  dating at the Minnesota Isotope Laboratory on the inductively coupled plasma mass spectrometers (ICP-MS, Thermo-Finnigan ELEMENT and Thermo Fisher NEPTUNE, ref. 35 and 36, respectively). The chemical procedures used to separate the uranium and thorium for  $^{230}\text{Th}$  dating are similar to those described in ref. 37.

Subsamples for stable isotope analysis were collected in two ways: 1) drilling with a dental drill bit of 0.5 mm in diameter directly from the polished half of the stalagmite at an average interval of 2mm, 1mm or 0.5mm along stalagmite axes, depending on sample growth rates; 2) cutting the stalagmite into a 1×0.5 cm slab using a diamond saw and then scraping off perpendicularly to the growth axes of the stalagmites at a mean resolution of ~20 subsamples per mm. The second method was applied for sections between 0 and 95 mm from the top of stalagmite XBL-29. We performed the stable isotopic analysis on all subsamples collected through the first method and every tenth sample from the second method. A total of 1896 oxygen isotopic values were

obtained on a Finnigan MAT-252 mass spectrometer equipped with Kiel Carbonate Device III at the Institute of Earth Environment, Chinese Academy of Sciences. International standard NBS19 and inter-laboratory standard TTB1 were run for every 10 to 15 samples and arbitrarily selected duplicate measurements were conducted every 10 to 20 samples, respectively, to check for homogeneity and reproducibility. All oxygen isotopic values are reported in  $\delta$  notation, the per mil deviation relative to the Vienna Pee Dee Belemnite (VPDB) standard ( $\delta^{18}\text{O} = [((^{18}\text{O}/^{16}\text{O})_{\text{sample}}/(^{18}\text{O}/^{16}\text{O})_{\text{standard}} - 1) \times 1000]$ ). Standard results show that the precision of  $\delta^{18}\text{O}_c$  analysis is better than 0.15‰ ( $2\sigma$ ).

### **Isotope-enabled GCM simulations**

The climate model used in this project incorporated HDO and  $\text{H}_2^{18}\text{O}$  into the NCAR CAM2. We then ran this isotope-enabled model with fixed sea surface temperature (SST) and sea ice distributions for the present-day and the LGM (38). SST in the Present Day run is given by the climatological monthly mean derived from observations from 1949 to 2001. In the LGM run, we used monthly SST and sea ice distribution simulated by the fully coupled atmosphere-land-ocean-ice Community Climate System Model (39) with atmospheric carbon dioxide ( $\text{CO}_2$ ), methane ( $\text{CH}_4$ ), and nitrous oxide ( $\text{N}_2\text{O}$ ) at 185 ppmv, 350 ppbv, and 200 ppbv respectively. The LGM ICE-5G reconstruction is used for the continental ice sheet extent and topography prescription. Surface ocean  $\delta^{18}\text{O}$  values for the present day and LGM are prescribed as 0.5‰ (40) and 1.7‰ (41), respectively. The isotope-CAM LGM simulation is initialized using the atmospheric state from the equilibrium simulation of the CCSM LGM run, and is integrated forward for 20 years using SSTs and glacial and sea ice extents from CCSM as boundary conditions. The present-day simulation was integrated for 15 years. In both cases, averages of the last 10 years were used for the analysis.

**Acknowledgments:** We thank Prof. P. Molnar and the reviewers for valuable suggestions. This work was supported by National Natural Science Foundation of China grants, National Basic Research Program of China, the Knowledge Innovation Program of the Chinese Academy of Sciences; U.S. National Science Foundation grants (EAR-0909195 and EAR-1211925 to I. Fung; EAR-0908792 and EAR-1211299 to R.L. Edwards and H. Cheng); Taiwan Ministry of Science

and Technology (MOST-103-2119-M-002-022 to C.-C. Shen) and a Singapore National Research Foundation fellowship.

## References:

1. Gadgil S (2003) The Indian monsoon and its variability. *Annu Rev Earth Planet Sci* **31**:429-467.
2. Prell WL, Kutzbach JE (1987) Monsoon variability over the past 150,000 years. *J Geophys Res* **92**:8411-8425.
3. Sirocko F, et al. (1993) Century-scale events in monsoonal climate over the past 24,000 years. *Nature* **364**:322-324.
4. Schulz H, Rad UV, Erlenkeuser H (1998) Correlation between Arabian Sea and Greenland climate oscillations of the past 110,000 years. *Nature* **393**:54-57.
5. Clemens SC, Prell WL (2003) A 350, 000 year summer-monsoon multi-proxy stack from the Owen Ridge, Northern Arabian Sea. *Marine Geology* **201**:35-51.
6. Gupta AK, Anderson DM, Overpeck JT (2003) Abrupt changes in the Asian southwest monsoon during the Holocene and their links to the North Atlantic Ocean. *Nature* **421**:354-357.
7. Cai YJ, et al. (2006) High-resolution absolute-dated Indian Monsoon record between 53 and 36 ka from Xiaobailong Cave, southwestern China. *Geology* **34**:621-624.
8. Cai YJ, et al. (2010) Large variations of oxygen isotopes in precipitation over south-central Tibet during Marine Isotope Stage 5. *Geology* **38**:243-246.
9. Wang YJ, et al. (2001) A high-resolution absolute-dated late Pleistocene monsoon record from Hulu cave, China. *Science* **294**:2345-2348.
10. Dykoski CA, et al. (2005) A high-resolution, absolute-dated Holocene and deglacial Asian monsoon record from Dongge Cave, China. *Earth Planet Sci Lett* **233**:71-86.
11. Cheng H, et al. (2009) Ice age terminations. *Science* **326**:248-252.
12. Berger A, Loutre MF (1991) Insolation values for the climate of the last 10 million years. *Quat Sci Rev* **10**:297-317.
13. Wang YJ, et al. (2008) Millennial- and orbital-scale changes in the East Asian monsoon over the past 224,000 years. *Nature* **451**:1090-1093.

14. Kim ST, O'Neil JR (1997) Equilibrium and nonequilibrium oxygen isotope effects in synthetic carbonates. *Geochim Cosmochim Acta* **61**:3461-3475.
15. Braconnot P, et al (2007) Results of PMIP2 coupled simulations of the Mid-Holocene and Last Glacial Maximum – Part 1: experiments and large-scale features. *Clim Past* **3**:261-277.
16. Kudrass HR, Hofmann A, Dose H, Emeis K, Erlenkeuser H (2001) Modulation and amplification of climatic changes in the Northern Hemisphere by the Indian summer monsoon during the past 80 k.y. *Geology* **29**:63-66.
17. Heinrich H (1988) Origin and consequences of cyclic ice rafting in the Northeast Atlantic Ocean during the past 130,000 years. *Quaternary Res* **29**:142-152.
18. An ZS, et al. (2011) Glacial-interglacial Indian summer monsoon dynamics. *Science* **333**:719-723.
19. Lu H, Zhang F, Liu X, Duce RA (2004) Periodicities of palaeoclimatic variations recorded by loess-paleosol sequences in China. *Quat Sci Rev* **23**:1891-900.
20. Wu Z, Huang NE (2009) Ensemble Empirical Mode Decomposition: a noise-assisted data analysis method. *Advances in Adaptive Data Analysis* **1**:1-41.
21. Wu Z, Huang NE, Long SR, Peng C-K (2007) On the trend, detrending, and variability of nonlinear and nonstationary time series. *Proceeding of the National Academy of Sciences USA* **104**, 14889-14894, doi: 10.1073/pnas0701020104.
22. Wu Z, Huang NE, Wallace JM, Smoliak BV, Chen X (2011) On the time-varying trend in global-mean surface temperature. *Climate Dynamics* **37**: 759-773, doi: 10.1007/s00382-011-1128-8.
23. Fleitmann D, et al. (2007) Holocene ITCZ and Indian monsoon dynamics recorded in stalagmites from Oman and Yemen (Socotra). *Quat Sci Rev* **26**: 170-188.
24. Sinha A, et al. (2005) Variability of Southwest Indian summer monsoon precipitation during the Bølling-Ållerød. *Geology* **33**:813-816.
25. Cai YJ, et al. (2012) The Holocene Indian monsoon variability over the southern Tibetan Plateau and its teleconnections. *Earth Planet Sci Lett* **335/336**:135-144.
26. Cheng H, Sinha A, Wang X, Cruz F, Edwards R (2012) The Global Paleomonsoon as seen through speleothem records from Asia and the Americas. *Clim Dynam* **39**:1045-1062.
27. Kutzbach JE (1981) Monsoon climate of the Early Holocene: Climate experiment with the Earth's orbital parameters for 9000 years ago. *Science* **214**:59–61.

28. Clemens SC, Prell WL, Sun Y (2010) Orbital-scale timing and mechanisms driving Late Pleistocene Indo-Asian summer monsoons: Reinterpreting cave speleothem  $\delta^{18}\text{O}$ . *Paleoceanography* **25**, PA4207, doi:4210.1029/2010PA001926.
29. Pausata FSR, Battisti DS, Nisancioglu KH, Bitz CM (2011) Chinese stalagmite  $\delta^{18}\text{O}$  controlled by changes in the Indian monsoon during a simulated Heinrich event. *Nat Geosci* **4**:474-480.
30. Maher BA (2008) Holocene variability of the East Asian summer monsoon from Chinese cave records: a re-assessment. *Holocene* **18**:861-866.
31. Dayem KE, Molnar P, Battisti DS, Roe GH (2010) Lessons learned from oxygen isotopes in modern precipitation applied to interpretation of speleothem records of paleoclimate from eastern Asia. *Earth Planet Sci Lett* **295**:219-230.
32. Lee JE, Fung I, DePaolo DJ, Henning CC (2007) Analysis of the global distribution of water isotopes using the NCAR atmospheric general circulation model. *J Geophys Res* **112**:D16306.
33. Liu TW, Tang W (2004) Oceanic influence on the precipitation in India and China as observed by REMM and QuikSCAT. Paper presented at The 2nd International Tropical Rainfall Measuring Mission Science Conference, Japan Aerospace Exploration Agency, Tokyo.
34. Peltier WR (2004) Global glacial isostasy and the surface of the ice-age Earth: The ICE-5G (VM2) model and GRACE. *Annu Rev Earth Planet Sci* **32**:111–149.
35. Shen C-C, et al. (2002) Uranium and thorium isotopic and concentration measurements by magnetic sector inductively coupled plasma mass spectrometry. *Chem Geol* **185**:165-178.
36. Cheng H, et al. (2013) Improvements in  $^{230}\text{Th}$  dating,  $^{230}\text{Th}$  and  $^{234}\text{U}$  half-life values, and U–Th isotopic measurements by multi-collector inductively coupled plasma mass spectrometry. *Earth Planet Sci Lett* **371**: 82–91.
37. Edwards RL, Chen JH, Wasserburg GJ (1987)  $^{238}\text{U}$ – $^{234}\text{U}$ – $^{230}\text{Th}$ – $^{232}\text{Th}$  systematic and the precise measurement of time over the past 500,000 years. *Earth Planet Sci Lett* **81**:175-192.
38. Lee JE, Fung I, DePaolo DJ, Otto-Bliesner B (2008) Water isotopes during the Last Glacial Maximum: new general circulation model calculations. *J Geophys Res* **113**:D19109.
39. Otto-Bliesner BL, et al. (2006) Last Glacial Maximum and Holocene climate in CCSM3. *J Climate* **19**:2526-2544.

40. Hoffmann G, Werner M, Heimann M (1998) Water isotope module of the ECHAM atmospheric general circulation model: a study on timescales from days to several years. *J Geophys Res* **103**:16871-16896.
41. Schrag DP, Hampt G, Murray DW (1996) Pore fluid constraints on the temperature and oxygen isotopic composition of the glacial ocean. *Science* **272**:1930-1932.
42. LeGrande AN, Schmidt GA (2009) Sources of Holocene variability of oxygen isotopes in paleoclimate archives. *Clim Past* **5**, 441-455.
43. DiNezio PN, et al. (2011) The response of the Walker circulation to Last Glacial Maximum forcing: Implications for detection in proxies. *Paleoceanography* 26, PA3217, doi:10.1029/2010PA002083.
44. Lee JE, et al. (2012) Asian monsoon hydrometeorology from TES and SCIMACHY water vapor isotope measurement and LMDZ simulations: Implications for speleothem climate record interpretation, *J. Geophys. Res.*, 117, D15112, doi:10.1029/2011JD-017133.
45. Battisti DS, Ding Q, Roe GH (2014) Coherent pan-Asian climate and isotopic response to precessional forcing, *J Geophys. Res.* (in revision)



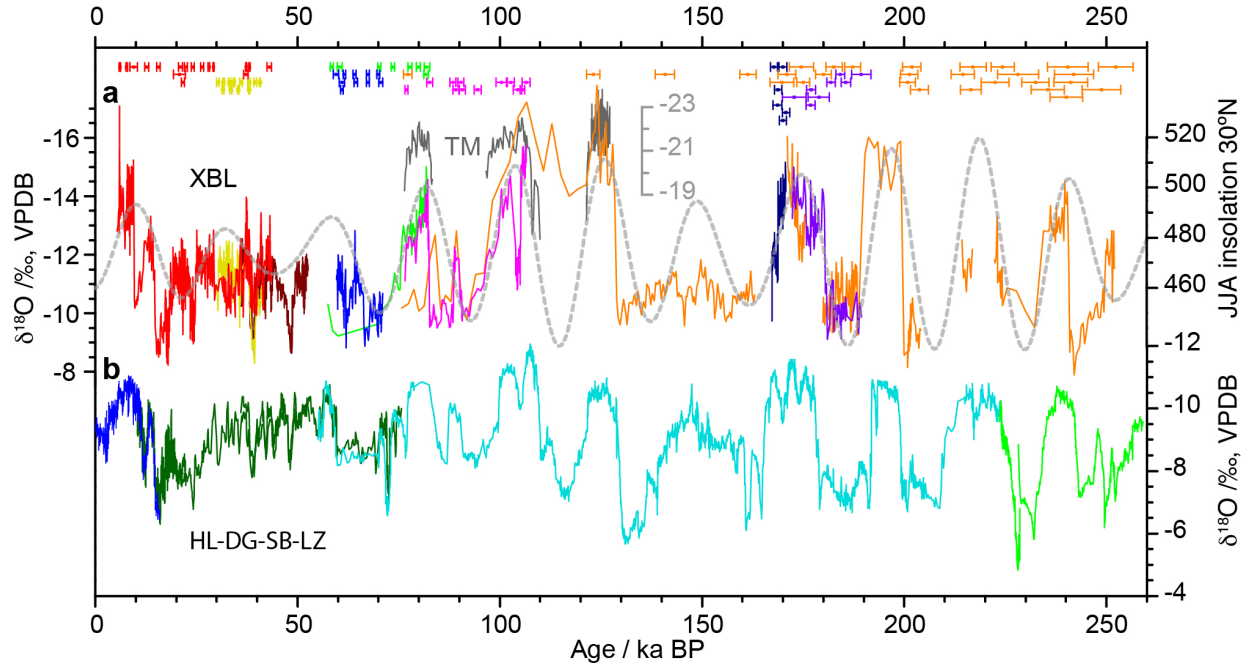


**Fig. 1.** (a) The  $\delta^{18}\text{O}_c$  record of the stalagmites from Xiaobailong cave: XBL-3 (yellow), XBL-4 (green), XBL-7 (blue), XBL-26 (orange), XBL-27 (violet), XBL-29 (red), XBL-48 (pink), XBL-65 (dark blue) and XBL-1 (purple, 7). The gray curve shows a previously established  $\delta^{18}\text{O}_c$  record from the Tibetan Plateau (Tianmen Cave), indicating ISM variations during Marine Isotope Stage 5 (8). The  $^{230}\text{Th}$  dates and errors ( $2\sigma$  error bars) are color-coded by stalagmites. (b) The  $\delta^{18}\text{O}_c$  records of Hulu cave (dark green, 9), Dongge cave (blue, 10), Sanbao cave (sky blue, 11), and Linzhu cave (light green, 11). The  $\delta^{18}\text{O}$  scales for all records shown are reversed (increasing downward). Summer insolation at  $30^\circ\text{N}$  (gray dashed line) is integrated over June, July, and August (12). VPDB - Vienna Peedee belemnite.

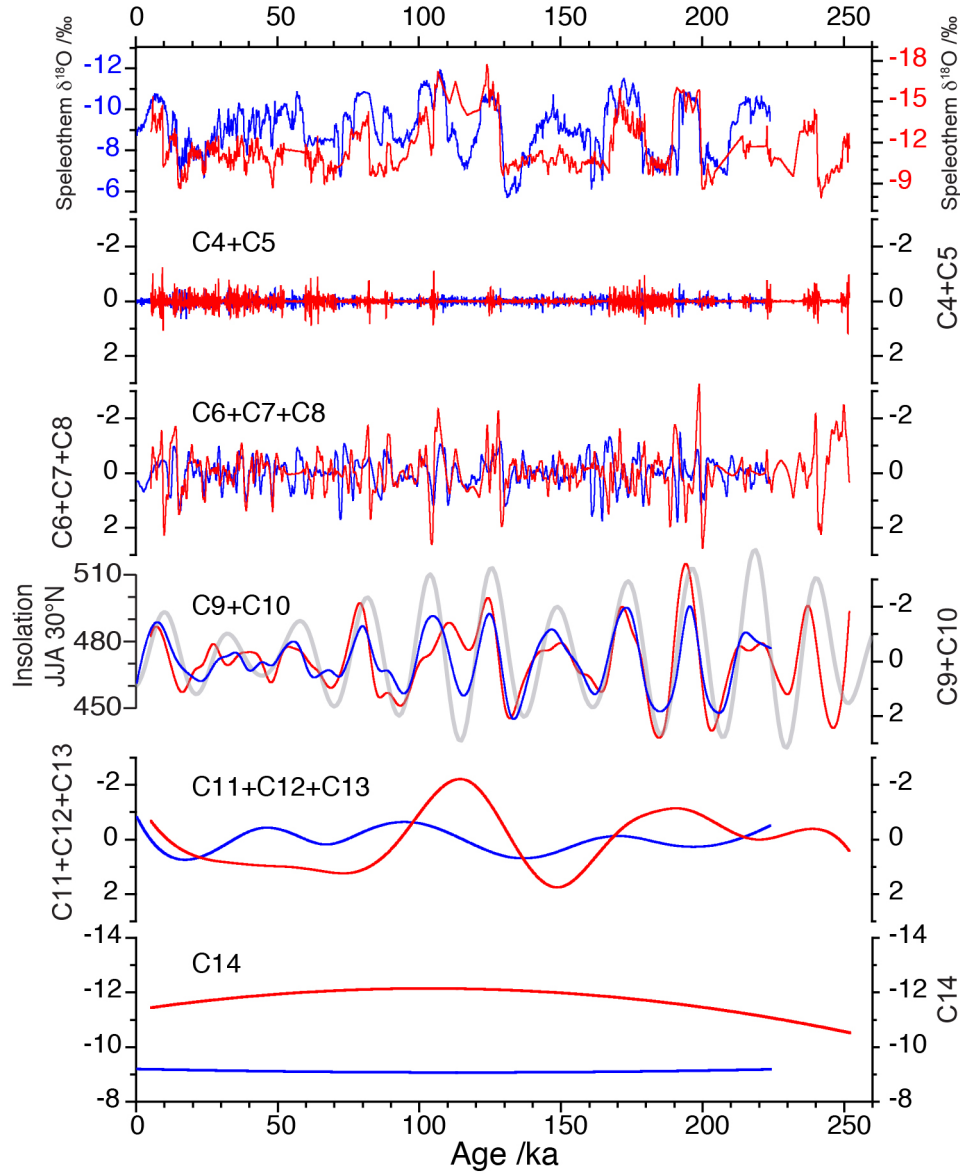


**Fig. 2.** EEMD components of the XBL (red) and Hulu-Dongge-Sanbao (blue) composite time series over the last 252 kyr. During decomposition, noise of 0.4 (0.2 standard deviation of the data) is added for the ensemble calculation, and the ensemble number is 300. Five EEMD components (i.e. sum of components 4-5, sum of components 6-8, sum of components 9-10, sum of components 11-13, and component 14) are presented. Component 14 indicates the overall trend. The individual components are shown in Supplemental Figure S9.

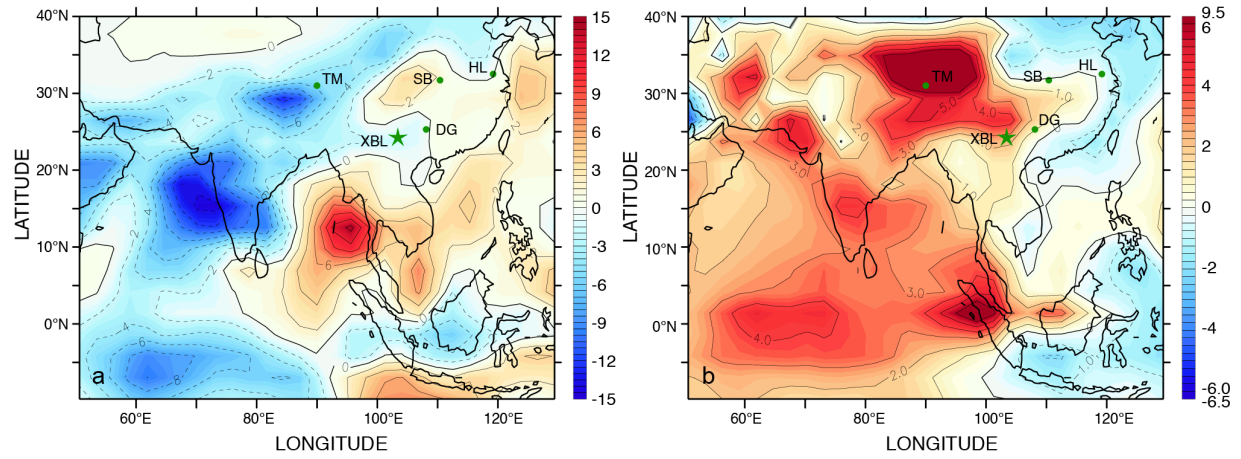


**Fig. 3.** Modeled difference (LGM minus present day) in June-July-August precipitation (mm/day, left panel) and amount-weighted precipitation  $\delta^{18}\text{O}_p$  (‰, right panel). Markers indicate the locations of the following caves: Xiaobailong (XBL), Hulu (HL), Dongge (DG), Sanbao (SB), and Tianmen (TM).

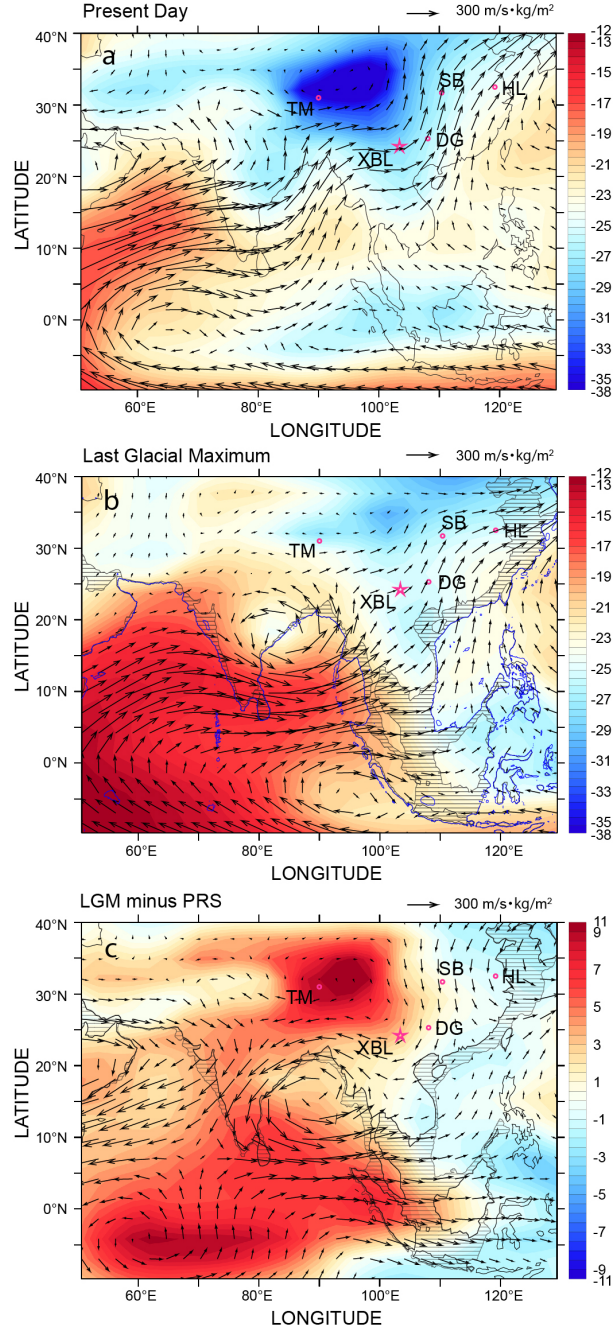


**Fig. 4.** Modeled June-July-August vapor transport (arrows,  $\text{m s}^{-1} \text{kg m}^{-2}$ ) and isotopic composition of column integrated vapor (color-shading, ‰) during the Present day (top panel), the LGM (middle panel) and the difference between LGM and Present day (bottom panel). Dark gray lines indicate the present coastline; the blue lines and hatched area in (b) indicate the coastline and the exposed continental shelf, respectively during the LGM when sea level was  $\sim 120\text{m}$  lower than present day. Markers indicate the locations of the following caves: Xiaobailong (XBL), Hulu (HL); Dongge (DG), Sanbao (SB), and Tianmen (TM).

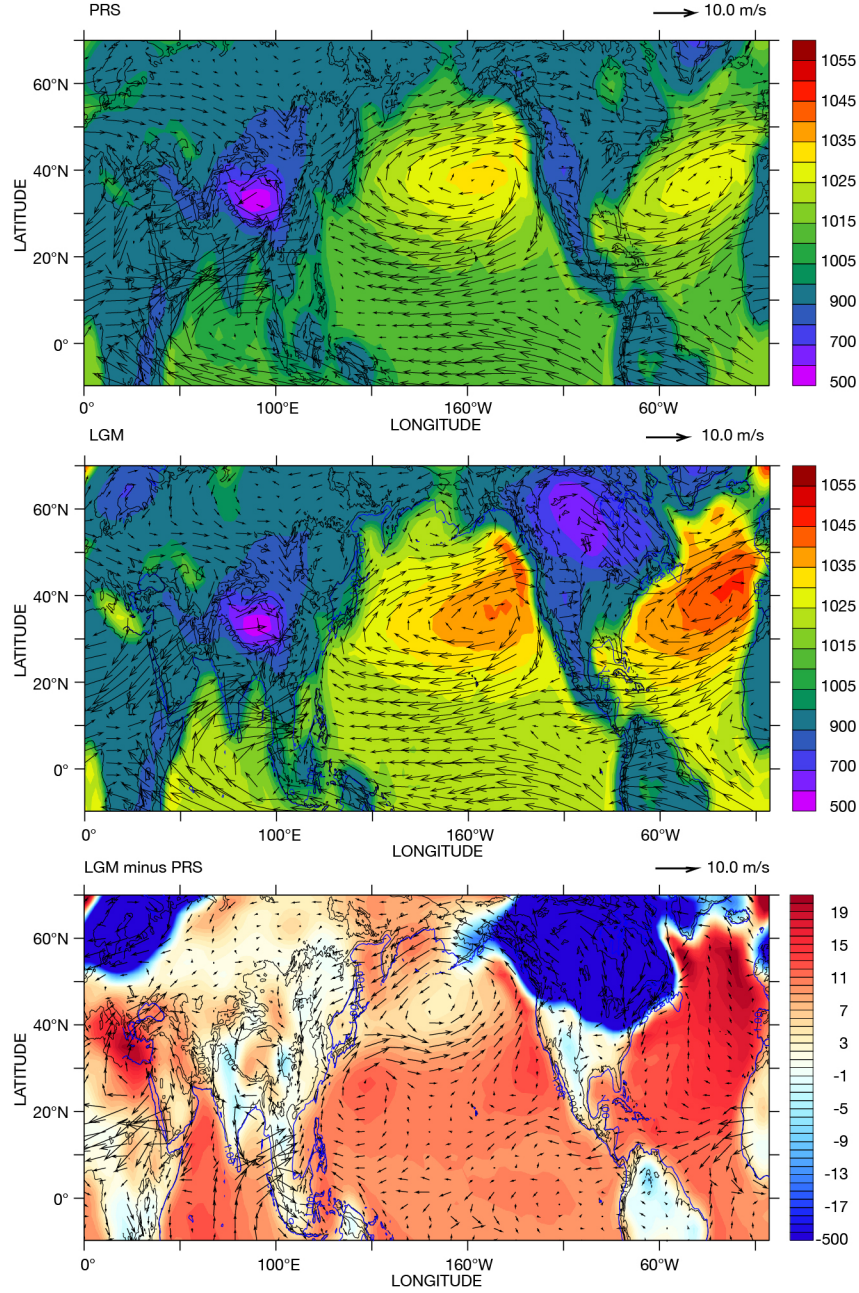


**Fig. 5.** Modeled June-July-August surface pressure for (a) the present-day and (b) the LGM, and (c) the departure of LGM surface pressure from the present day (color, hPa). The arrows denote the corresponding near-surface winds (averaged over the lowest 4 layers, ~300 hPa thick, of the model atmosphere). Topography (meters) is contoured. The thick blue line denotes the LGM coastline with a 120-meter drop in sea level.